Energy distributions of He^+ and He_2^+ ions formed in ultracold $He(2\,^3S_1)+He(2\,^3P_2)$ collisions

M. Pieksma,* M. Čížek,† J. W. Thomsen,‡ P. van der Straten, and A. Niehaus
Debye Institute, Department of Atomic and Interface Physics, Utrecht University, P.O. Box 80000, 3508 TA Utrecht, The Netherlands
(Received 25 January 2002; published 9 August 2002)

Energy distributions of He^+ and He_2^+ ions produced in ultracold $He(2\,^3S_1)+He(2\,^3P_2)$ collisions are presented. These helium metastable atoms are trapped and cooled in a magneto-optical trap, and have a temperature of 1.1 ± 0.2 mK. Initial kinetic energies of the product He^+ and He_2^+ ions are analyzed in energy, using a weak electrostatic extraction field in combination with a time-of-flight technique. A pronounced structure is observed in the He^+ ion distribution, which can be well explained by a theoretical model that considers the avoided crossings between only three metastable $^3\Sigma_g^+$ states of the transient He_2 molecule. The measured He_2^+ distribution has a width that is consistent with the maximum recoil energy of 1.1 meV.

DOI: 10.1103/PhysRevA.66.022703 PACS number(s): 34.50.Gb, 33.20.−t

I. INTRODUCTION

Laser-cooling and -trapping techniques [1] have greatly advanced the experimental exploration of purely quantum-mechanical effects in ultracold atomic collisions. By creating cold, dense, as well as well-localized and well-prepared atomic samples, the sensitivity and resolution of pre-laser-cooling era experiments could be superseded by a spectacular many orders of magnitude. For instance, important progress has been reported in the study of long-range interactions between atoms [2,3]. The interaction of two metastable helium atoms provides a particularly good probe of the quantum nature of collisions, since it is a symmetric, few-electron system. Resonances in the elastic-scattering cross section and in the electron- and ion-energy distributions of ionizing metastable helium collisions depend very sensitively on the potential-energy curves. This makes it possible to gather knowledge of these curves from experiment directly, which has been a long-time goal in experimental collision physics.

Penning ionization plays a dominant role in ultracold metastable atom collisions. In the Penning process the internal energy in the collision systems is so high that during the close encounter of the two atoms sufficient energy is present that an electron can be emitted. Since the process leads to deexcitation of one atom and to ionization of the other, Penning ionization is a large loss process for traps of metastable atoms and therefore this process also bears relevance for the Bose-Einstein condensation studies. Violation of spin conservation reduces the ionization probability of the quintet state by several orders of magnitude. Penning ionization has been studied for He [4–10], Kr [11], and Xe [12], but in all cases only the total ionization rate has been detected.

The helium metastable collision system has served as a fundamental test case in ''conventional'' atomic collision physics for many years. At thermal and subthermal collision energies, Müller *et al.* [13] carried out pioneering experiments on metastable helium collisions. Electron-energy distributions were measured at 1.6 and 61 meV, and a pronounced (oscillatory) structure was observed. A theoretical treatment employing *ab initio* potential-energy curves, and a quantum-mechanical method based on complex potential theory [14], provided a good description of the experimental results. At the lowest collision energy studied, fast oscillations were seen that could be traced back to interference between incoming and outgoing heavy particle waves in the entrance channel. In contrast, this paper opens up the realm of the ultracold temperature regime. Measurements of ion-energy distributions (which directly reflect the electron-energy distributions) are presented and interpreted, yielding information on the potential-energy curves (and symmetries) involved.

The interaction of two metastable helium atoms was studied at a temperature of 1.1 ± 0.2 mK [5], which corresponds to a collision energy of only 140 neV. This was realized by trapping, cooling, and confining the metastable helium atoms (He^*) in a magneto-optical trap (MOT). The following processes were investigated:

$$He(2\,^3S_1)+He(2\,^3P_2)\rightarrow\begin{cases}He^+ + He(1\,^1S)+e^-,\\ He_2^+ + e^-.\end{cases}\qquad(1)$$

The first process represents Penning ionization (PI), and the second represents the associative ionization (AI) [15]. Below, collisions of the type of Eq. (1) will be referred to as $S+P$ collisions. In the case both atoms are in the $He(2\,^3S_1)$ state, the reaction will be referred to as $S+S$ collisions.

II. EXPERIMENT

A. Experimental setup

The experimental setup is shown schematically in Fig. 1. A liquid-helium-cooled discharge source produces metastable helium atoms with a mean velocity of around 300 m/s.

*Present address: Nederlands Meetinstituut, Department of Temperature and Radiation, Ionizing Radiation Section, P.O. Box 80000, 3508 TA Utrecht, The Netherlands. Email address: mpieksma@nmi.nl

†Present address: Institute of Theoretical Physics, Faculty of Mathematics and Physics, Charles University Prague, V Holešovičkách 2, 18000 Praha 8, Czech Republic.

‡Present address: Niels Bohr Institute, Orsted Lab, Universitatsparken 5, DK 2100 Copenhagen O, Denmark.

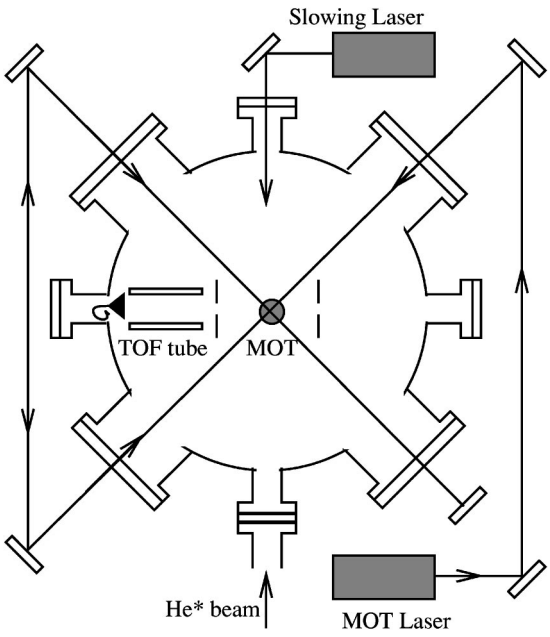

FIG. 1. Schematic drawing of the MOT experimental setup.

This atomic beam is Zeeman slowed on the $D2$ transition in the magnetic field of the MOT. The MOT laser (being the most critical component of the setup for a stable MOT operation) is frequency locked at a red detuning of 10Γ using saturated absorption spectroscopy [16]. The slowing laser was operated at a red detuning of 29.5Γ, and could optionally be frequency locked as well to obtain very good long-term (many hours) stability. Both lasers are diode lasers manufactured especially for the $S+P$ transition at 1083 μm. The intensities of the laser beams correspond to a saturation parameter $s_0=50-100$ for the MOT laser and $s_0=400$ for the slowing laser. Specific details on the experimental setup in general and the operation of the MOT in particular (e.g., with respect to the proper polarization of the recirculated MOT laser beam, and the magnetic-field gradient generated by anti-Helmholtz coils) can be found in Refs. [5,17]. Here it suffices to mention that typically 10^6 atoms can be trapped inside a volume of about 4 mm^3 (1 mm radius of the atomic sample), yielding a density of 2.5×10^8 atoms per cm^3.

The MOT laser is switched ''on'' and ''off'' with a 50% duty cycle and a 10-kHz repetition rate. In the ''on'' period the laser is close to resonance and the atoms are cooled and trapped in the MOT (see Fig. 2). In the ''off'' period the laser is detuned far from resonance, so in this period the atoms are effectively untrapped and are in the ground state. By sweeping this laser quickly through resonance during the ''off'' period, a well-defined starting time was generated for $S+P$ collisions. During a period of several microseconds before and after the starting time, the slowing laser was switched ''off.'' This helped to reduce the continuous background signal, which was due to $S+S$ collisions. The He^+ and He_2^+ ions produced by $S+P$ collisions during the fast (less than 0.2 μs) swept laser pulse were mass and energy selected using a time-of-flight (TOF) technique. The TOF geometry is such that the ions are first accelerated by a weak electrostatic

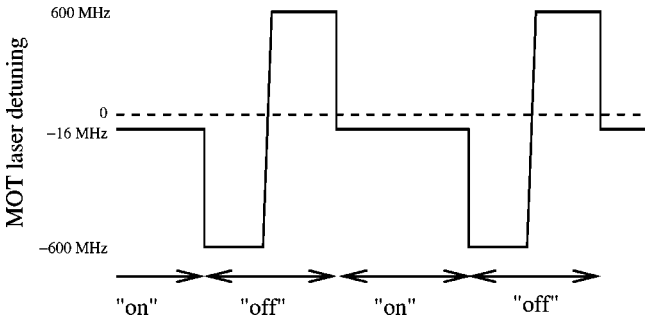

FIG. 2. Schematic diagram of the timing sequence for the experiment. In the ''on'' period (50 ms) the MOT laser is close to resonance and the atoms are trapped and cooled. In the ''off'' period (50 ms) the laser is far detuned from resonance and the atoms are not trapped and are in the ground state. During the ''off'' period the laser is scanned quickly through resonance and this creates ions due to $S+P$ collisions, which are synchronized with the sweep of the laser through resonance.

field (about 1 V/cm for He^+ measurements, while a weaker field of about 0.25 V/cm was used for He_2^+ measurements for improved resolution [18]) and then postaccelerated into a TOF tube at the end of which a channeltron detector is located. The second acceleration stage allows time-of-flight focusing and total count rate optimization. The total path length is 295 mm. In Fig. 3 the ion spectrometer is depicted schematically.

Simultaneously with the scanning of the MOT laser a time-to-amplitude-convertor (TAC) is started. The ions detected by the channeltron detector provide the stops for the TAC. The TAC output signal is sent to a multichannel analyzer, which is controlled using a personal computer (PC). Data are stored digitally for further analysis on the PC.

B. Data transformation

Ion-energy distributions are obtained by a transformation of the measured TOF distributions, using the proper Jacobian. Background signal due to $S+S$ collisions and autoionizing reactions of He* with rest gas is uncorrelated to the swept laser pulse that induces the $S+P$ collisions. Therefore it is continuous and structureless. This background signal is

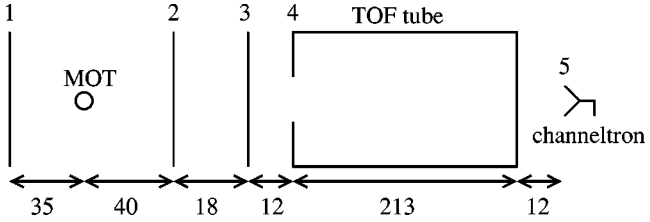

FIG. 3. Schematic representation of the geometry of the ion time-of-flight spectrometer (not to scale, all distances are in millimeters). The dot indicates the position of the MOT. Grid 1 has a diameter of 26 mm, grids 2 and 3 have a diameter of 27 mm, and the TOF tube has an outer diameter of 30 mm. The entrance aperture of the TOF tube (position 4) has a diameter of 7.5 mm. The following potentials are applied: $V_1=0$ V, $V_2=V_3=-10.51$ V, $V_4=-33.1$ V, and $V_5=-2400$ V.

corrected for by making a linear fit to that part of the TOF spectrum that does not contain any $S+P$ signal. The primary maximum in the He^+ TOF spectra corresponds to ions with zero kinetic energy. Smaller times of flight indicate energetic ions ejected in the direction of the detector, while larger times of flight are for ions that are initially emitted in the opposite direction, and are then slowed down and have their trajectories turned around by the electrostatic field. Since the latter ions spend more time in the acceleration region, the resolution for this part of the spectrum is intrinsically enhanced. The count rate in the tails of the ion distribution is suppressed, because the transmission of the ions through the spectrometer decreases with ion energy. This means that in the measurement the statistical uncertainty increases with increasing initial ion kinetic energy.

C. Effect of MOT magnetic field on ion trajectories

It should be mentioned that the MOT magnetic field has a gradient of 15 G/cm, which can affect the ion trajectories. However, the magnetic-field lines point radially outward in the symmetry plane, which is defined as the plane that has one axis along the slowing laser beam line and the other one along the axis of the spectrometer. Ions traveling in this plane in the direction of detector experience no deflection. Only those ions that are ejected under a significant angle with the symmetry plane and that have an initial kinetic energy large compared to the electrostatic energy picked up during acceleration are deflected. In our case, the recoil energy of the He_2^+ ions is so small that all of them will be collected, while the maximum initial kinetic energy of the He^+ ions is well below 1 eV, which is much less than the several tens of eV's of electrostatic energy these ions acquire. Of the He^+ ions that do suffer considerable magnetostatic deflection the majority would never have made it to the detector even without the presence of the magnetic field. Careful alignment of the setup was needed to ensure that the effect of the magnetic field was indeed small. So, no correction was made for magnetostatic deflection.

D. Simulations of ion trajectories

In order to relate the measured times of flight of the detected ions to their initial kinetic energies, one needs to know exactly the electrostatic acceleration these ions have experienced. A complication is that in our setup the size of the MOT laser puts constraints on the possible sizes and spacings of the electrostatic grids. The diameters of the grids used are less than the spacing of the grids around the interaction region. This implies that no homogeneous electrostatic field could be realized, and so no straightforward relationship exists between the distance from the interaction center and the electric-field strength. The algorithms of the SIMION [19] software package were used to tackle this problem. SIMION solves the Laplace equation given certain boundary conditions for any configuration of electrodes. The whole setup, including the vacuum chamber, was modeled accurately using the actual sizes, distances, and electrostatic potentials of all equipment present inside this chamber. The SIMION calculations established the connection between the time of flight of the ions and their initial kinetic energy. Also, a Monte Carlo simulation program was written for SIMION to calculate the transmission of the spectrometer for both ion species as a function of this initial kinetic energy. This program utilized random ejection angles and starting positions from inside a fixed sample volume. A distinction was made between ion ejected in either the forward or the backward direction with respect to the direction in which the detector is located.

The position of the atomic sample along the spectrometer axis was adjusted slightly in the SIMION calculation, so that the time of flight of He^+ ions with zero initial kinetic energy coincided with the actual maximum of the experimental He^+ TOF distribution. This is a completely legitimate procedure, since one can observe directly in the experiment that, depending on the actual alignment and detuning of the diode lasers, the position of the atomic sample may vary by a few millimeters.

III. THEORY

In their comprehensive paper, Müller *et al.* [13] studied the energies of electrons released in PI and AI processes in $He^*(2\,^3S)+He^*(2\,^3S,2\,^1S)$ collisions both theoretically and experimentally. They used the local complex potential (LCP) approximation to describe the heavy particle motion [14]. Employing the projection operator technique they calculated the lowest potential-energy curves with $^1\Sigma_g^+$, $^3\Sigma_u^+$, and $^5\Sigma_g^+$ symmetry, where g and u stand for the gerade and ungerade symmetry, respectively. They also obtained *ab initio* decay widths of some of these states towards the two ionization continua $He_2^+(^2\Sigma_u^+)+e^-$ and $He_2^+(^2\Sigma_g^+)+e^-$. It is known that the LCP approximation works well for metastable states lying high in the continuum [20]. The validity and breakdown of the LCP approximation as the discrete states approach or enter the continuum threshold has been studied in Refs. [21,22]. The LCP approximation has previously been used to study PI and AI of metastable helium atoms [13,23].

For the treatment of the $He^*(2\,^3S)+He^*(2\,^3S)$ collisions only the $1^1\Sigma_g^+$ and $1^3\Sigma_u^+$ states are important, as ionization via the $1^5\Sigma_g^+$ state is forbidden due to spin conservation [13]. Since these two states have different reflection symmetries, the problem can be separated in two parts, where only one state interacts with the continuum. For the treatment of the $He^*(2\,^3S)+He^*(2\,^1S)$ collisions more than one state with the same symmetry contributes to the electron spectrum and these states display curve crossings in the region of interest for the electron emission process. Müller *et al.* [13] treated this problem in a simplified way by using the semiclassical Landau-Zener model, thus neglecting the phase information in contributions of the probability amplitude from the different states.

In this paper we study the energy spectrum of the ions produced in $He^*(2\,^3S)+He^*(2\,^3P)$ collisions. Due to energy conservation the electron spectrum for this process can easily be transformed into the He^+ energy spectrum. Since there is no information about the molecular states with Π and $^1\Sigma$ symmetry connected to this asymptote, we cannot completely model the electron energy spectrum for a direct

comparison with the experimental results. However, information about the state with $^3\Sigma_g^+$ symmetry is known. It displays curve crossings with lower-lying states of the same symmetry. Therefore we have to solve the Schrödinger equation within the LCP approximation for several coupled channels. To our knowledge this problem has not yet been studied in the context of PI, but it has been treated for electron-molecule collisions [24] and for collisions of atoms with metal surfaces [25].

Local coupled complex potentials treatment

The projection operator approach to the theory of PI and the use of the LCP approximation is derived elsewhere (see Refs. [13,14,26] and references therein). In the Born-Oppenheimer approximation the motion of the metastable helium atoms in the entrance channel is described by the wave function $\psi_*^J(R)$ (R is the internuclear distance). It is the solution of the radial Schrödinger equation (atomic units are used throughout this section)

$$\left(-\frac{1}{2\mu}\frac{\mathrm{d}^2}{\mathrm{d}R^2}+\frac{J(J+1)}{2\mu R^2}+V_*(R)+F_J\right)\psi_*^J(R)=E_*\psi_*^J(R), \tag{2}$$

with J being the angular momentum in the heavy particle motion, $V_*(R)$ being the potential energy of the discrete state, and F_J being the level shift operator resulting from the interaction of the discrete state with the continuum (see below). The radial wave function $\psi_+^J(R)$ representing the product molecule He_2^+ or the dissociating $He+He^+$ is given by a similar equation for the exit channel, where the potential V_*+F_J is replaced by the interaction potential V_+ for the ionic system.

Before discussing the calculation of the electron-energy spectrum we will first describe the potentials involved in more detail. For the $He+He^+$ asymptote there are two states of $^2\Sigma_g^+$ and $^2\Sigma_u^+$ symmetry connected. The potential-energy curves have been calculated by a number of authors [27] and we have used spline interpolation of the data of Broeke [28]. Since the two states of different symmetry are not coupled, we can solve the Schrödinger equation for each of the two states separately. We will denote the respective wave functions with ψ_{+u} and ψ_{+g}.

The situation is more complicated for the metastable channel. The shape of the $2^3\Sigma_g^+$ potential connected to the $He^*(2\,^3S)+He^*(2\,^3P)$ asymptote indicates avoided crossings [13], which makes it necessary to consider two additional potential curves of the $^3\Sigma_g^+$ symmetry. We will denote by U_i the potential energy of the $i^3\Sigma_g^+$ adiabatic state, with $i=1,2,3$. For the Born-Oppenheimer approximation we have to transform these three potentials into a diabatic representation,

$$V_*\equiv\begin{pmatrix} V_1(R) & C_{12}(R) & C_{13}(R)\\ C_{21}(R) & V_2(R) & C_{23}(R)\\ C_{31}(R) & C_{32}(R) & V_3(R)\end{pmatrix}$$
$$=M^T\begin{pmatrix} U_1(R) & 0 & 0\\ 0 & U_2(R) & 0\\ 0 & 0 & U_3(R)\end{pmatrix}M, \tag{3}$$

where M is a unitary matrix. The Hermitian matrix of the diabatic potentials and couplings V_* enters Eq. (2) for the three-component wavefunction $\psi_{*i}(R)$.

Information on the matrix V_* can be extracted from the data for the potentials $U_i(R)$ published in Ref. [13]. We assume a Morse potential function for the diabatic potentials,

$$V_i(R)=A_i(e^{-\alpha_i(R-R_i)}-1)^2-A_i+E_i, \quad i=2,3, \tag{4}$$

with E_i being the asymptotic energies of each potential relative to the $He+He^+$ asymptote. For the first potential $V_1(R)$

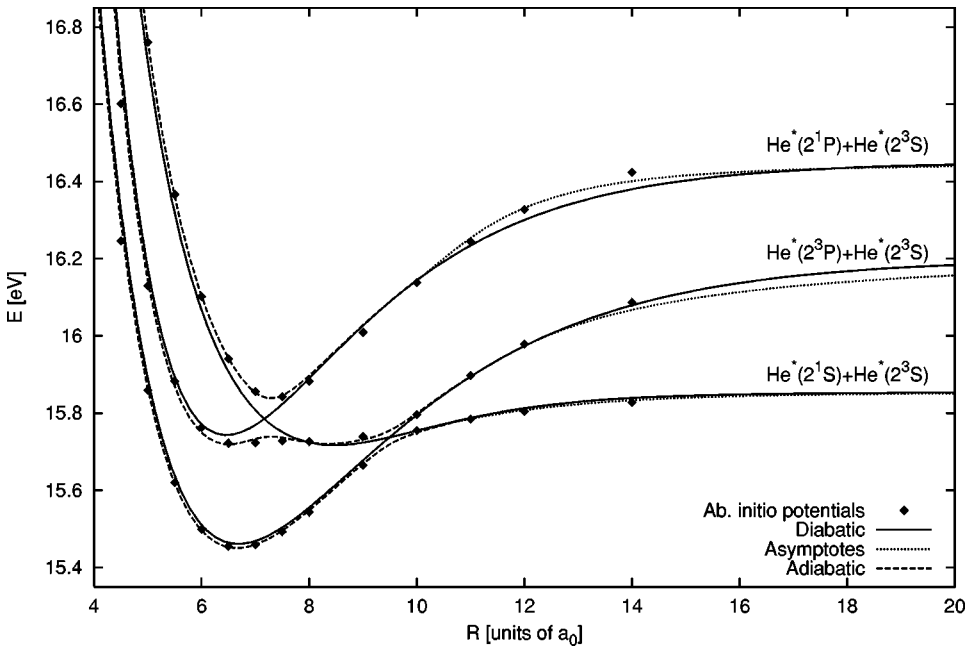

FIG. 4. Diabatic potential-energy curves of the helium metastable $^3\Sigma_g^+$ quasimolecular states (solid lines) relevant for the present study. The dotted line shows corrections that incorporate the correct long-range behavior. The dashed lines are the corresponding adiabatic potential-energy curves, while the diamonds represent the *ab initio* data [5].

TABLE I. Parameters describing the Morse function for the $i\,^3\Sigma_u$ potentials connected to the $He(2\,^3S)-He(2\,^3S,2\,^1S,2\,^3P)$ asymptotes for models $\mathcal{A}$ and $\mathcal{B}$ (see text). Energies are in units of eV, whereas distances are in units of a_0.

	i	E_i	A_i	α_i	R_i	B_i	β_i	X_i	
Model $\mathcal{A}$	1	15.854	0.2031	0.9379	$\equiv R_2$				$b=7528$
	2	16.2	0.7392	0.3362	6.682	1.381	0.4582		$c=7.269$
	3	16.45	0.7071	0.3948	6.46	$\equiv B_2$	$\equiv \beta_2$		$d=33.59$
Model $\mathcal{B}$	1	15.854	0.2394	0.8931	$\equiv R_2$				$b=7996$
	2	16.2	0.7506	0.3368	6.65	0.0103		9.48	$c=7.223$
	3	16.45	721.5	0.3982	6.414	0.0566		7.16	$d=33.95$

the minimum is too shallow to be represented accurately by the Morse function and we have added an additional term vanishing as R^{-6} at infinity,

$$V_1(R)=A_1e^{-\alpha_1(R-R_1)}-b[(R-c)^2+d]^{-3}+E_1. \quad (5)$$

For the couplings we assume

$$C_{12}(R)=C_{13}(R)=Be^{-\beta R} \quad (6)$$

and $C_{23}=0$, since the two curves $V_2(R)$, $V_3(R)$ do not cross. The adiabatic potentials U_i for each R are the solutions of the algebraic equation

$$\begin{vmatrix} x-V_1(R) & C_{12}(R) & C_{13}(R) \\ C_{12}(R)^* & x-V_2(R) & C_{23}(R) \\ C_{13}(R)^* & C_{23}^*(R) & x-V_3(R) \end{vmatrix}=0, \quad (7)$$

where the constants are chosen in such a way that the three roots $x=U_i$ are the best least-squares fits to the data of Müller *et al.* [13]. The resulting values are given in the Table I under model $\mathcal{A}$. The resulting diabatic potentials $V_i(R)$ are depicted in Fig. 4 together with the adiabatic curves U_i and the *ab initio* data of Müller *et al.* [13]. The diabatic curves $V_i(R)$ obtained with this procedure are quite accurate, because the curves lie near the adiabatic *ab initio* data except in the vicinity of the crossings, where they switch from one curve to another.

Although the *ab initio* data provide sufficient information about the couplings $C_{12}(R)$ and $C_{13}(R)$ at the crossings, they yield little information about the couplings far from the crossings and no information on the phase of the coupling. To test our assumptions regarding the detailed form of the couplings, we have constructed a second model (model $\mathcal{B}$), where the coupling are given by

$$C_{1i}=B_ie^{-(R-X_i)^2}, \quad i=2,3. \quad (8)$$

Here the parameters X_i are obtained from the crossing points of the *ab initio* data by linear interpolation. The parameters for the best fit are also shown in Table I. Note, that although the couplings in two models differ significantly over the whole range of distances R, they are approximately equal at the crossing.

The Morse functions do not have the correct van der Waals behavior for large R. The values of the C_6 and C_8 coefficients for the $1\,^3\Sigma_g^+$ potential are given in Ref. [13]. The values of C_3 for the other two $^3\Sigma_g^+$ states $V_2(R)$ and $V_3(R)$ are determined by the dipole moment of the $2\,^3S$-$2\,^3P$ transition in He and are given by $C_3=12.83$ and 2.93 a.u., respectively. In order to join the potentials at short and large distance smoothly at a matching distance R_m, we have added terms to the long-range potential,

$$V_i=\sum_{n=3,6,8,10,12}\frac{C_{i,n}}{R^n}, \quad (9)$$

where the values $C_{i,n}$ are given in Table II.

Each of the three $^3\Sigma_g^+$ states is coupled to the continuum by the coupling element $W_{ij}(R)$, where the subscript i refers to one of the three discrete states (in the diabatic representation) and $j=u,g$ refers to gerade or ungerade final state of He_2^+ ion. Since we have no information on the complex phase of the coupling we will simply assume that W_{ij} is a real quantity. The *nonlocal* level shift operator F is given by

TABLE II. Long-range dispersion coefficients for the $i\,^3\Sigma_u$ potentials connected to the $He(2\,^3S)-He(2\,^3S,2\,^1S,2\,^3P)$ asymptotes. The first dispersion coefficients are determined from theoretical values and the other coefficients are values fitted to obtain the best matching with the short-range potentials at the matching distance R_m. Values are for model $\mathcal{A}$. For model $\mathcal{B}$ the parameters are identical, apart from $R_m=10.8$ for $V_3(R)$.

i	C_3 (a.u.)	C_6 (10^3 a.u.)	C_8 (10^5 a.u.)	C_{10} (10^8 a.u.)	C_{12} (10^9 a.u.)	R_m a_0
1		−5.839	−4.194	+1.0325	−3.9594	10
2	−12.83	+1.5295	−6.0928			12
3	−2.93			−3.5278	+26.949	10

$$F\psi_* = \sum_j \int dR F_{ij}(R,R')\psi_{*j}(R), \tag{10}$$

where

$$F_{ij}(R,R') = \int d\epsilon \sum_n W_{in}(R)[E - T_N - \epsilon - V_{+n}(R) + i\varepsilon]^{-1} W_{jn}(R'). \tag{11}$$

In general, the coupling W_{ij} depends on the energy of the released electron. In our case, the dependence on ϵ can be removed according to the Franck-Condon principle for the conservation of the total electronic energy $\epsilon(R) = V_*(R) - V_+(R)$ during a vertical transition. In the LCP approximation the nonlocal energy-dependent operator F is replaced by a local quantity. Furthermore, since the coupling is weak [13], the real part of this quantity can be neglected. We thus obtain for the *local* level shift operator F,

$$F\psi_* = -\frac{i}{2} \sum_{jn} \Gamma^n_{ij}(R)\psi_{*j}(R), \tag{12}$$

where the decay widths Γ^n_{ij} are defined by

$$\Gamma^n_{ij}(R) \equiv 2\pi W_{in}(R) W_{jn}(R). \tag{13}$$

The local level shift operator F is thus fully determined by the decay widths Γ^n_{ii} of the three autoionizing $i\ ^3\Sigma_g^+$ states towards the two continua $n = u,g$. Nondiagonal elements are then obtained from the relation $\Gamma^n_{ij} = \sqrt{\Gamma^n_{ii}\Gamma^n_{jj}}$. However, we have no *ab initio* information about the decay widths Γ^n_{ii} for the $^3\Sigma_g^+$ states. We therefore use as suggested in Ref. [13] a single width function for all channels and we have chosen the same width as for the He*$(2\ ^3S)$+He*$(2\ ^3S)\ 1\ ^3\Sigma_g^+$ channel. We performed test calculations which indicate that the shape of the electron spectrum is not that sensitive to the width functions.

The Schrödinger equations for the metastable and ionic state are solved numerically on a grid of typically several thousands of points on an interval $R = 0a_0 - 30a_0$. The method for the numerical solution of the complex coupled channel problem is described in detail in Ref. [26]. Finally, the electron spectra are obtained from

$$\frac{d\sigma}{d\epsilon} = \frac{2}{E_* \sqrt{E_* E_+}} \sum_{Jf} (2J+1) \left| \sum_i T_J^{(fi)}(E_+, E_*) \right|^2 \tag{14}$$

for PI $(E_+ > 0)$ and

$$\sigma^J_{\nu_f} = \frac{2\pi}{E_* K_*} (2J+1) \left| \sum_i T_J^{(fi)}(E^J_{\nu_f}, E_*) \right|^2 \tag{15}$$

for associative ionization into a final bound state with the energy $E^J_{\nu_f}$. Contributions to the T matrix are

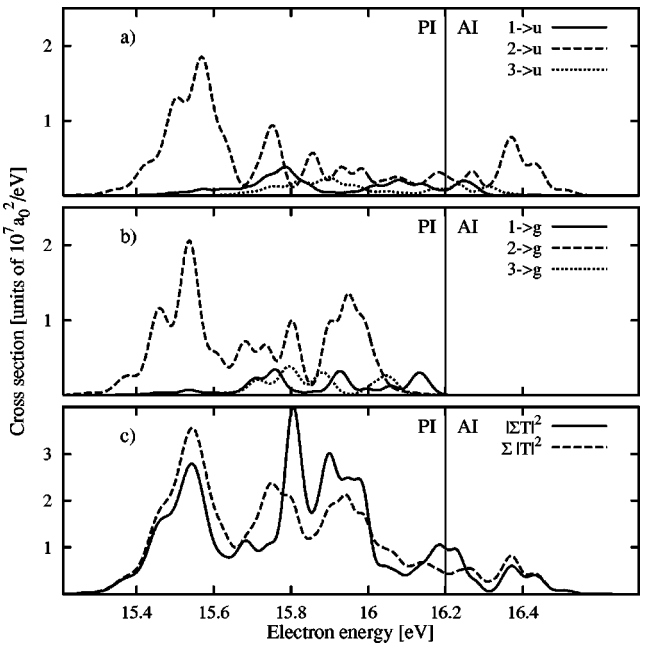

FIG. 5. Simulated electron spectrum for model $\mathcal{A}$. (a) and (b) show individual contributions from different potential-energy curves. (c) shows the coherent (solid line) and incoherent (dashed line) sums of all contributions.

$$T_J^{(fi)}(E_+, E_*) = \int dR' \ \psi^J_{+f}(E_+, R') W_{if}(R) \psi^J_{*i}(E_*, R'), \tag{16}$$

where $\epsilon_f = E_* - E_+$ is the energy of the electron released in the ionization process and $K_* = \sqrt{2\mu E_*}$.

IV. COMPARISON OF EXPERIMENT AND THEORY

We have calculated the electron spectrum for a collision energy of $E = 10^{-7}$ eV. The terms with $J < 13$ have been included in the sum of Eq. (14) in order to get convergence in the results. Only terms with even values of J are included for the homonuclear molecular system with gerade symmetry. Convolution of the electron spectrum with a Gaussian function of the 35 meV width (full width at half maximum) has been performed to simulate in part the finite resolution in experiments.

The results for the model $\mathcal{A}$ are presented in Fig. 5, where parts (a) and (b) show the contributions of the individual T-matrix elements to the spectrum. The repulsive $^2\Sigma_g^+$ state of He_2^+ does not support bound states and the part of the spectrum corresponding to associative ionization is not present for the final state of gerade symmetry. The state connected to He*$(2\ ^3S)$+He*$(2\ ^3P)$ asymptote ($i = 2$, i.e., the dashed curve) gives the largest contribution to spectrum. It is well known from semiclassical considerations [23] that the difference between the onset of the electron spectrum and the associative ionization threshold is closely related to the potential well depth of the difference potential $V_*(R) - V_+(R)$ and the high-energy end of the spectrum is closely related to the potential difference $V_*(R_T) - V_+(R_T)$ at the

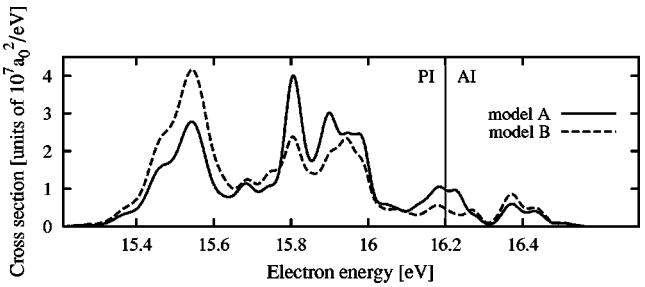

FIG. 6. Comparison of the electron spectra for the two models $\mathcal{A}$ and $\mathcal{B}$.

classical turning point R_T of the potential $V_*(R_T)=E_*$. In our case of coupled channels, the contribution from each channel also lies approximately within these bounds, although the spectrum for $i=1$ (solid line) extends to somewhat lower energies due to coupling with the $i=2$ state.

The resulting simulated electron spectrum (solid line) for cold $He^*(2\,^3S)+He^*(2\,^3P)$ collisions is shown in Fig. 5(c). To show the importance of the relative phase of the individual T-matrix elements we also show the spectrum calculated with an ''incoherent sum'' of the T-matrix elements $\Sigma_i|T^{(fi)}|^2$ instead of the proper expression $|\Sigma_i T^{(fi)}|^2$ in Eq. (14) for the cross section. If the influence of the states with $i=1$ and 3 is only marginal, the two curves in Fig. 5(c) should be nearly identical. It is apparent that although the contribution of the $i=2$ state is dominant, the influence of the other two states (including the proper complex phase) on the behavior of the final spectrum is not negligible. This is also demonstrated in Fig. 6. Here the spectrum for the models $\mathcal{A}$ and $\mathcal{B}$ are compared. Note, that the models differ only slightly in the potentials and the main difference is in the diabatic couplings among the discrete states far from the crossings. The exponential behavior of the coupling in model $\mathcal{A}$ overestimates the coupling at short distances.

The theoretical electron-energy distributions are converted to ion-energy distributions in a straightforward manner, using conservation of energy and momentum,

$$E_{\rm ion}=\frac{E_2-\epsilon}{2}, \tag{17}$$

with E_2 the asymptotic energy, as given in Table I. Here an electron energy $\epsilon=E_2$ indicates the limit above which associative ionization occurs (see Figs. 5 and 6).

In Fig. 7(a) the experimental and theoretical results for model $\mathcal{A}$ are shown for the backward ejected He^+ ions, and in Fig. 7(b) for the forward ejected He^+ ions. Preliminary results of the present experiment have been published in Ref. [29], but without the present resolution, and did not yet reveal the detailed structure observed here. Figure 7(a) has the highest resolution, while Fig. 7(b) serves as a very useful indicator for the reliability of the experimental procedure. Even the result of the low-resolution measurement shown in the latter figure already reveals the main features of the ion distribution.

According to Fig. 7(a), a good overall agreement between the experimental ion-energy distribution and the incoherent

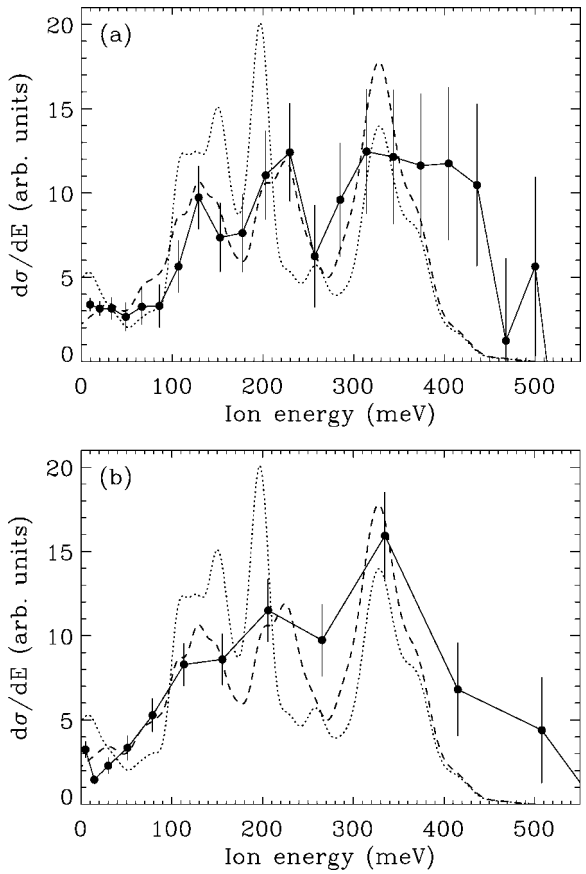

FIG. 7. Energy distributions of the He^+ ions (a) ejected in the backward direction with respect to the detector position, and (b) ejected in the forward direction in 140 neV metastable helium collisions. The filled dots are the experimental results. The dashed lines were obtained from the theoretical calculations for model $\mathcal{A}$, as described in the text. The long-dashed line shows the incoherent theoretical spectrum; the short-dashed line shows the coherent theoretical spectrum. Error bars have been added to several experimental points to give an impression of the statistical uncertainties in different parts of the spectrum. The height of the theoretical curves is simply scaled by eye to obtain a satisfactory overall agreement with the experiment, and is kept the same in both figures.

theoretical result is obtained, although this becomes somewhat worse at the higher energies. In view of the larger statistical uncertainties in that energy region, this is acceptable. From a closer comparison with the theoretical result, we see that the widths and positions of the three peaks that we observe [see Fig. 7(a)] are also well reproduced (again, especially at the lower energies). The height of the peaks is strongly influenced by the competition between the channels, as can be seen in Fig. 5. According to Fig. 7(a), there is no clear evidence in the experimental results for interference between these channels, since the incoherent theoretical spectrum agrees better with the measured ion distribution than does the coherent theoretical spectrum. In the theoretical spectrum we only take the three $^3\Sigma_g^+$ quasimolecular states into account to explain the measured ion-energy distribution. The effect of the other states, for example the Π states, cannot be determined by us, since no information on their potentials is available.

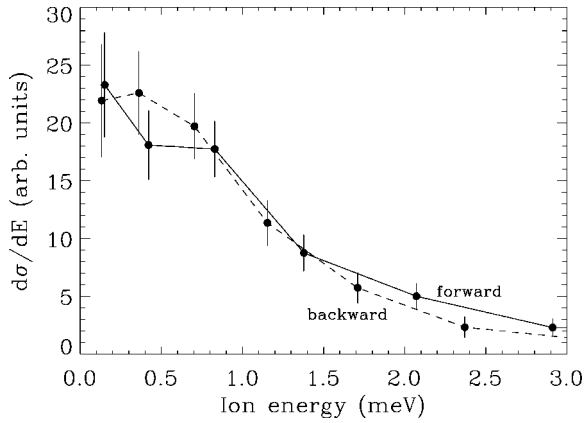

FIG. 8. Energy distributions of the He_2^+ ions, consisting of the spectra of both the forward (solid line) and backward (dashed line) ejected ions. The error bars represent statistical uncertainties.

In Fig. 8 the experimental ion-energy distributions of the He_2^+ ions are presented. Both the spectra for forward (2π solid angle) and backward (2π solid angle) ejected ions are shown, which appear to coincide very well. This is exactly what one should expect for low ion energies on the order of only 1 meV. From the measurements the full width at half the maximum of the distributions is extracted, which yields a value of 1.18 ± 0.25 meV. The width is caused by the recoil of the ions due to the emission of the electron and the finite resolution of the detector. A straightforward calculation based on conservation of energy and momentum gives a maximum recoil energy of 1.10 meV. The finite resolution of the experiment is caused by spatial variations in the formation of the He^{2+} ions within the MOT cloud and the finite duration of the swept laser pulse. The resolution is hard to quantify, but we estimate it to be of the order of 1 meV. The combination of the two effects is consistent with the measured width. Finally, note that the absolute error bars in Fig. 8 get smaller with smaller cross sections (still, the relative uncertainties increase). This is due to the very low background signal rate when using very weak electrostatic fields.

V. CONCLUSIONS

In conclusion, oscillatory features have been observed in the He^+ ion-energy distribution of ultracold $S+P$ metastable helium collisions. These features can be well explained by theoretical calculations based on a semiclassical formulation that considers avoided crossings between relevant channels. The positions of the maxima in the ion-energy distribution approximately reflect the well depth of the different participating entrance channels of the collision. No significant interference between these channels seems present. It is quite remarkable that the good agreement between the experimental and theoretical results is established by using only states with $^3\Sigma_g^+$ symmetry.

In addition, energy distributions have been presented for the He_2^+ ions. By using very small electrostatic extraction fields a meV energy resolution was achieved for these molecular ions. This measurement confirmed the maximum theoretical recoil energy of 1.1 meV. Finally, we have demonstrated that the combination of a MOT and a TOF technique provides a powerful experimental tool.

ACKNOWLEDGMENTS

The authors would like to acknowledge technical support by Ing. J. van der Weg and stimulating discussions with Dr. D. van Oosten. This work was part of the research program of the ''Stichting voor Fundamenteel Onderzoek der Materie'' (FOM), which was financially supported by the ''Nederlandse Organisatie voor Wetenschappelijk Onderzoek'' (NWO). M.C. would like to acknowledge Grant No. GAČR 203/00/D111 from the Grant Agency of the Czech Republic.

[1] H. Metcalf and P. van der Straten, Phys. Rep. **244**, 203 (1994).
[2] P.D. Lett, P.S. Julienne, and W.D. Phillips, Annu. Rev. Phys. Chem. **46**, 423 (1995).
[3] J. Weiner, V.S. Bagnato, S. Zilio, and P.S. Julienne, Rev. Mod. Phys. **71**, 1 (1999).
[4] F. Bardou, O. Emile, J.-M. Courty, C.I. Westbrook, and A. Aspect, Europhys. Lett. **20**, 681 (1992).
[5] H.C. Mastwijk, M. van Rijnbach, J.W. Thomsen, P. van der Straten, and A. Niehaus, Eur. Phys. J. D **4**, 131 (1998).
[6] M. Kumakura and N. Morita, Phys. Rev. Lett. **82**, 2848 (1999).
[7] P.J.J. Tol, N. Herschbach, E.A. Hessels, W. Hogervorst, and W. Vassen, Phys. Rev. A **60**, R761 (1999).
[8] N. Herschbach, P.J.J. Tol, W. Vassen, W. Hogervorst, G. Woestenenk, J.W. Thomsen, P. van der Straten, and A. Niehaus, Phys. Rev. Lett. **84**, 1874 (2000).
[9] A. Browaeys, J. Poupard, A. Robert, S. Nowak, W. Rooijakkers, E. Arimondo, L. Marcassa, D. Boiron, C.I. Westbrook, and A. Aspect, Eur. Phys. J. D **8**, 199 (2000).
[10] F. Pereira Dos Santos, F. Perales, J. Léonard, A. Sinatra, Junmin Wang, F. Saverio Pavone, E. Rasel, C.S. Unnikrishnan, and M. Leduc, Eur. Phys. J. D **14**, 15 (2001).
[11] H. Katori and F. Shimizu, Phys. Rev. Lett. **73**, 2555 (1994).
[12] M. Walhout, U. Sterr, C. Orzel, M. Hoogerland, and S.L. Rolston, Phys. Rev. Lett. **74**, 506 (1995).
[13] M.W. Müller, A. Merz, M.-W. Ruf, H. Hotop, W. Meyer, and M. Movre, Z. Phys. D: At., Mol. Clusters **21**, 89 (1991).
[14] R.J. Bieniek, Phys. Rev. A **18**, 392 (1978).
[15] A. Niehaus, Phys. Rep. **186**, 149 (1990).
[16] W. Lu, D. Milic, M.D. Hoogerland, M. Jacka, K.G.H. Baldwin, and S.J. Buckman, Rev. Sci. Instrum. **67**, 3003 (1996).
[17] H.C. Mastwijk, Ph.D. thesis, Utrecht University, 1997.
[18] The initial kinetic energies of the He^{2+} ions are much less than those of the He^+ ions. By using a weaker electrostatic field an improved resolution could be realized without loss of He^{2+} signal.
[19] SIMION 3D software program, version 6.0, Princeton Electronic Systems, 1995.
[20] M. Movre and W. Meyer, J. Chem. Phys. **106**, 7139 (1997).

[21] H. Morgner, Chem. Phys. **145**, 239 (1990).

[22] R.J. Bieniek, J. Phys. B **13**, 4405 (1980).

[23] R.J. Bieniek, M.W. Müller, and M. Movre, J. Phys. B **23**, 4521 (1990).

[24] H. Estrada, L.S. Cederbaum, and W. Domcke, J. Chem. Phys. **84**, 152 (1986).

[25] G.E. Makhmetov, A.G. Borisov, D. Teillet-Billy, and J.P. Gauyacq, Nucl. Instrum. Methods Phys. Res. B **100**, 342 (1995).

[26] M. Čížek, Ph.D. thesis, Charles University, Prague, 2000. Available in the electronic version at http://otokar.troja.mff.cuni.cz/~cizek

[27] J.N. Bardsley, Phys. Rev. A **3**, 1317 (1971); A.K. Khan and K.D. Jordan, Chem. Phys. Lett. **128**, 386 (1986); C.W. Bauschlincher, Jr., H. Partridge, and D. Ceperley, *ibid.* **160**, 183 (1989); J. Ackerman and H. Hogreve, Chem. Phys. **157**, 75 (1991).

[28] R. Broeke, Master's thesis, Universiteit Utrecht, The Netherlands, 1998.

[29] G. Woestenenk, H.C. Mastwijk, J.W. Thomsen, P. van der Straten, M. Pieksma, M. van Rijnbach, and A. Niehaus, Nucl. Instrum. Methods Phys. Res. B **154**, 194 (1999).